2007

Polarization Reversal in Potassium Titanyl Phosphate

William D. Mitchell
Wright State University

Polarization Reversal in Potassium Titanyl Phosphate

A thesis submitted in partial fulfillment of the requirements for the degree of
Master of Science

By

William David Mitchell
B.S., Suffolk University, 2001

2007
Wright State University

WRIGHT STATE UNIVERSITY

SCHOOL OF GRADUATE STUDIES

November 5, 2007

I HEREBY RECOMMEND THAT THE THESIS PREPARED UNDER MY SUPERVISION BY William David Mitchell ENTITLED Spontaneous Polarization Reversal in Potassium Titanyl Phosphate BE ACCEPTED IN PARTIAL FUFILLMENT OF THE REQUIREMENTS FOR THE DEGREE OF Master of Science.

_____
Lok C. Lew Yan Voon, Ph.D.
Thesis Advisor and Department Chair

_____
Joseph F. Thomas, Jr., Ph.D.
Dean of the School of
Graduate Studies

Committee on Final Examination

_____
Lok C. Lew Yan Voon, Ph.D.

_____
David E. Zelmon, Ph.D.

_____
Jerry D. Clark, Ph.D.

Abstract

Mitchell, William David. M.S., Department of Physics, Wright State University, 2007. Polarization Reversal in Potassium Titanyl Phosphate.

Polarization reversal in both hydrothermal and flux grown potassium titanyl phosphate was studied using square pulses at room temperature from 1600 V/mm to 5000 V/mm. Maximum switching current and inverse switching time data is compared to the ferroelectric polarization reversal model developed by Fatuzzo and Merz in the last century. Room temperature calculation of spontaneous polarization is reported and compared to that of potassium titanyl phosphate in the literature.

Contents

List of figures

List of Tables

Chapter 1 Introduction

Potassium titanyl phosphate ($KTiOPO_4$, KTP) is a ferroelectric crystal used in many nonlinear optical applications such as frequency doubling of lasers. Ferroelectric crystals have an inherent polarization which is reversible by the application of an external electric field. The reversal of polarization by an electric field is known as electric field poling. The poling may be done in a manner to create regions of adjacent anti-parallel polarization known as domains. These back to back regions (domains) of opposite polarization give rise to a process known as quasi phase matching (QPM) within the crystal which produces second harmonic generation of light (frequency doubling).

Early work on polarization reversal (switching) in ferroelectrics was done by Fatuzzo and Merz in the 1950s[1,2]. Their interest in ferroelectrics was for use as computer memory elements. The ability to switch between opposite polarization states allows for the representation of the binary elements 0 and 1. Fatuzzo and Merz studied studied various ferroelectrics including barium titanate ($BaTiO_3$) try-glycine sulfate (TGS). These studies led Fatuzzo and Merz to propose a model for the switching time and maximum switching current during polarization reversal in ferroelectrics.

This thesis attempts to apply the model developed by Fatuzzo and Merz to potassium titanyl phosphate during polarization reversal. The question is whether the model developed by Fatuzzo and Merz applies to KTP. The motivation for this work is not only an attempt to validate the Fatuzzo and Merz model, but also to provide some

basic information regarding switching time and switching current in KTP as it may aid those using KTP for optical or computer memory applications.

Switching time and maximum switching current during polarization reversal for applied fields from 1600 V/mm – 5000 V/mm in both flux grown and hydrothermal grown KTP was studied. Spontaneous polarization calculated from switching current versus time data is compared to spontaneous polarization values found in the literature.

The thesis is organized as follows. Chapter 2 covers background theory on ferroelectric crystals. Chapter 3 gives the crystal structure and some of the properties of KTP. Chapter 4 presents the switching time and maximum switching current models developed by Fatuzzo and Merz. Chapter 5 describes the samples, the experimental apparatus and procedure. Chapter 6 provides the results of the inverse switching time, maximum switching current, and calculated spontaneous polarization. Chapter 7 provides conclusions drawn from this research, namely does KTP follow the model developed by Fatuzzo and Merz, and suggests some future work to be done on polarization reversal in KTP.

Chapter 2 Ferroelectric Crystals

2.1 Definition of a ferroelectric crystal

Ferroelectric crystals have a spontaneous polarization (an inherent electric dipole moment) in the absence of an external electric field which may be switched between two polar equilibrium states by the application of an external electric field. The equilibrium states have the same crystal structure, but differ in the direction of the polarization. The electric field required to switch between the polarization states is called the coercive field.

Most ferroelectrics have what is known as a phase transition temperature called the Curie point, T_c. Below the Curie point, ferroelectrics are said to be in the pyroelectric (polar) phase. Pyroelectric cystals are ones in which a change in the spontaneous polarization may be brought about by a temperature differential. Above the Curie point ferroelectric crystals are said to be in the paraelectric (non-polar) phase. In the paraelectric phase ferroelectricity disappears due to thermal motion. Some ferroelectric crystals have no Curie point. That is, they melt and decompose before ever reaching a paraelectric phase. However, before melting they still possess the reversible polarization of the pyroelectric phase and are therefore considered ferroelectrics.

Ferroelectric crystals that posses a Curie point may be classified into two groups: displacive and order-disorder. For displacive ferroelectrics the atomic displacements above the Curie point will go from oscillations about a nonpolar site to oscillations about

a polar site. For order-disorder ferroelectrics the atomic displacements will go from a multi-well configuration to an ordered subset of the multi-well sites. These displacement transitions can be defined by the character of the transition in terms of the dynamics of the lowest frequency optical phonon. If the lowest frequency phonon can propagate in the crystal at the Curie point then the transition is displacive. If, however, the lowest frequency phonon can not propagate at the Curie point, that is it is diffusive, there is really no phonon, but only a large amplitude hopping motion between the wells and the transition is order-disorder. Some ferroelectrics have low frequency phonons that fall between these two transitions at the Curie point.

The displacive class of ferroelectrics includes ionic crystals related to the perovskite and ilmenite structures. The order-disorder class of ferroelectrics includes crystals with hydrogen bonds in which the motion of the protons is related to the ferroelectric properties. Table 2.1 shows some common ferroelectric crystals with their Curie points and spontaneous polarizations.

Table 2.1[3].Various ferroelectric crystals with their Curie points and spontaneous polarizations

		T_C in K	P_S in $\mu C/cm^2$ (at T in K)
KDP type	KH_2PO_4	123	4.75 (96)
	KD_2PO_4	213	4.83 (180)
	RbH_2PO_4	147	5.6 (90)
	KH_2AsO_4	97	5.0 (78)
	GeTe	670	--
TGS type	Try-glycine sulfate	322	2.8 (29)
	Try-glycine selenate	295	3.2 (283)
Pervoskites	$BaTiO_3$	408	26.0 (296)
	$KNbO_3$	708	30.0 (523)
	$PbTiO_3$	765	>50.0 (296)
	$LiTaO_3$	938	50
	$LiNbO_3$	1480	71 (296)

2.2 Displacive transitions

Two view points contribute to an understanding of ferroelectric displacive transitions: polarization catastrophe and condensation of a transverse optical phonon (Kittel, Introduction to Solid State Physics, 7^{th} edition). In a polarization catastrophe, the local electric field caused by the ionic displacement is larger than the elastic restoring force, thereby giving an asymmetric shift in the position of the ions. Higher order restoring forces will limit the shift to a finite displacement. For optical phonon condensation, that is condensation in the Bose-Einstein sense, there is a time-independent displacement of finite amplitude. This occurs when the corresponding transverse optical phonon frequency vanishes at some point in the Brillion zone. Longitudinal optical phonons have higher frequencies than transverse optical phonons of the same wave vector and their condensation may be neglected.

In either case, the formation of electric dipoles within the ferroelectric crystal is physically due to a relative displacement between cations and anions in the crystal structure. For example, look at the structure of barium titanate (see figure 2.1). Here, the Ba^{2+} and Ti^{4+} cations are displaced relative to the O^{2-} anions giving rise to a dipole moment. This displacement is found for temperatures below the Curie temperature and is formed during the growth process.

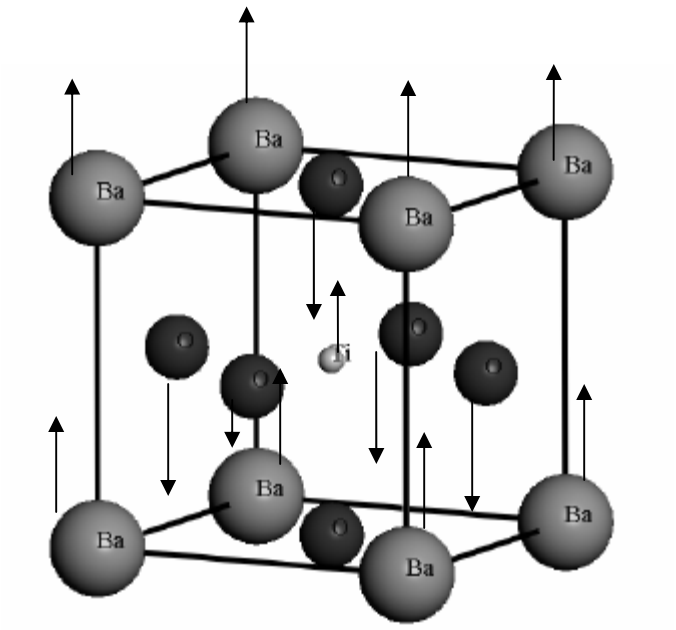

Figure 2.1. The crystal structure of barium titanate. Ti^{4+} and Ba^{2+} ions shifted in opposite direction of O^{2-} ions.

2.3 Ferroelectric hysteresis

A key characteristic of ferroelectrics is the plot of polarization vs. applied electric field (see figure 2.2).

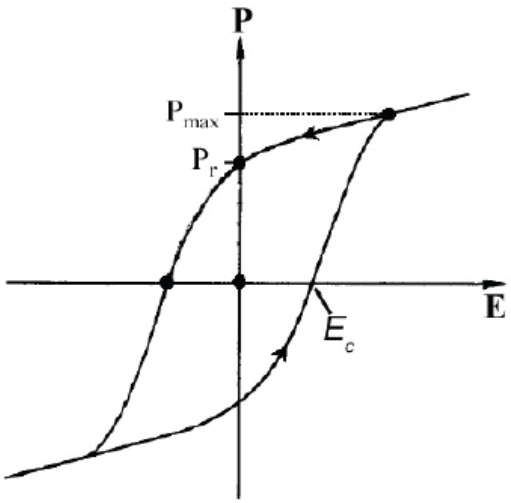

Figure 2.2[4] . A typical hysteresis loop for a ferroelectric.

In figure 2.2, $\mathbf{P}_{max}$ is the spontaneous polarization, $\mathbf{P_r}$ is the remnant polarization and $\mathbf{E_c}$ is the coercive filed. In principle the spontaneous polarization is equal to the saturation value of the electric displacement extrapolated to zero. The remnant polarization is the displacement at zero field and may be different from the spontaneous polarization if reverse nucleation occurs before the applied field reverses. This can happen either in the presence of internal or external stress or if the free charges below the crystal surfaces can not reach their new equilibrium distribution during each half cycle of the loop. At very low and very high electric fields a ferroelectric crystal behaves like an ordinary dielectric with a high dielectric constant. At the coercive field, polarization reversal takes place and gives rise to a large dielectric non-linearity. The area within the hysteresis loop is a measure of the energy required to reverse the polarization twice. At zero field, the polarization has two values corresponding to the opposite orientations of the spontaneous polarization.

2.4 Polarization reversal

In order to bring about polarization reversal one needs to overcome the depolarizing field within the crystal. An externally applied electric field creates charges on the surface of the crystal. The field produced in the interior of the crystal by these surface charges is called the depolarizing field because it acts in opposition to the applied field as well as the spontaneous polarization. By minimizing this field, or rather compensating for it, one can enable the transition between polar states. There are two factors involved in the compensation: internal screening of the bulk material and the external screening of the circuit used to provide the applied field to the crystal.

According to the Landauer[5] model of polarization reversal, minimizing the depolarization energy plays a crucial role in polarization reversal. The general equation for the screening charge is

$$Q_{\Sigma} = Q_{bo}(1 - e^{-\tau_{sw}/\tau}) + \int_{0}^{\tau_{sw}} J_{ext}\, dt\,, \tag{2.1}$$

where the first term is the bulk free compensating charge due to a finite conductivity of a ferroelectric and the second term, Q_{ext}, is the charge from the external source through the electrodes by the current J_{ext} . Q_{bo} is the total free space charge, τ_{sw} is the polarization switching time, and $\tau = \varepsilon\varepsilon_o/\sigma$ is the dielectric relaxation time (ε is the dielectric permittivity; σ is the dc conductivity). During polarization switching, a displacement current flows in the crystal while a transient current J_{ext} flows in the external circuit. If the switching time is much less than the dielectric relaxation time then the first term in equation 2.1 may be neglected.

2.5 Domains

In the absence of an external field, the direction of the spontaneous polarization in an ideal ferroelectric crystal can arise with equal probability along several crystal-ographic directions of the prototype paraelectric phase. The regions of the crystal with uniformly oriented spontaneous polarization are called domains. Boundaries that separate regions of different orientations are called domain walls. A domain wall is a

narrow region in which the crystalline structure is disturbed. It is generally believed that in ferroelectric crystals domain formation consists of domain nucleation followed by forward (parallel to the applied field) and sideways (perpendicular to the applied field) growth of the domain through the crystal.

Miller and Wienreich[6] developed an equation for the domain wall velocity (forward growth) which may be written as

$$v = v_{\infty} \exp(-\alpha b^{3/2}), \tag{2.2}$$

where b is the lattice constant and α is a constant depending on the parameters of the two dimensional nuclei, the applied field density, and the temperature. Equation 2.2 indicates that the smaller the lattice constant the larger the domain wall velocity.

The equation for calculation of the activation energy of a nucleus formation was developed by Landauer[5] and is

$$\Delta F = -2EP_S V + \sigma_w A + \frac{1}{2} N P_S^2 V \tag{2.3}$$

where the first term is the energy of interaction between the P_s and the applied electric field E. The volume of the nucleus is V. The second term is the nucleus surface energy with A as the domain wall area. The last term is the energy of the depolarizing field, caused by the divergence of polarization along the domain boundary. N is the depolarization factor.

2.6 Crystal defects

Defects in any crystal lattice generally cause deformation of the surrounding volume and modification of the local fields. For example, assume a defect has a dipole moment $\Delta\boldsymbol{\mu}$. If the defect concentration, N, is low enough so that the interaction between them can be neglected, the macroscopic polarization change is

$$\Delta\mathbf{P} = N\Delta\boldsymbol{\mu} \,. \tag{2.4}$$

During the poling process, the $\Delta\mathbf{P}$ due to the defects may or may not reverse. If it does reverse, then the coercive field will depend on both the field required to switch the defects and the sign and magnitude of $\Delta\mathbf{P}$. In general, the presence of defects tends to increase the coercive field. Defects may induce the existence of frozen-in nuclei, small regions in which the preferred direction of $\mathbf{P}_s$ is never changed. There are also defects that prefer a particular orientation of $\mathbf{P}_s$ causing back-switching of the dipoles after the external field is removed. The formation and migration of defects during the poling process might be responsible for observed phenomena known as crystal fatigue. It has been noticed that upon repeated switching of ferroelectric crystals, most notably in barium titanate[4], that the spontaneous polarization becomes clamped and the coercive field increases.

Chapter 3 Properties and Growth of KTP

3.1 Introduction

The first reported growth of potassium titanyl phosphate, $KTiOPO_4$, was in 1890 by L. Ouvard[7]. However, it was not until the 1970's when KTP became known as a nonlinear optical material. Bierlien *et al.*[8] reported the first KTP waveguides using ion exchange in molten nitrates of Rb, Cs, and Tl. In 1990, Van der Poel *et al*.[9] reported highly efficient SHG by domain inversion resulting from ion exchange. During the 1990's, several groups reported bulk periodic poling in KTP by various techniques such as room temperature electric field poling, electron beam patterning, low temperature poling and chemical patterning.

Compared with lithium niobate ($LiNbO_3$), a competing nonlinear optical material, KTP has a lower nonlinearity but a greater resistance to optical damage and photorefraction. Also, KTP's coercive field (2.1 kV/mm)[10] is an order of magnitude lower than $LiNbO_3$ (21 kV/mm)[11], and its anisotropic structure limits domain broadening.

3.2 Crystal Structure

KTP belongs to a family of compounds that have the formula unit $MTiOXO_4$, where M can be K, Rb, Tl, NH_4, or Cs and X can be either P or As. Solid solutions exist among the various members of the family, with only slight changes in lattice parameters. All members of the family are orthorhombic and belong to the a-centric point group mm2

and space group $Pna2_1$. For KTP the lattice constants[12] are a = 12.814 Å, b = 6.404 Å, and c = 10.616 Å.

The KTP structure is characterized by helical chains of distorted TiO_6 octahedra that are corner linked and separated by PO_4 tetrahedra. The TiO_6 octrahedra along the c-axis bridge the PO_4 tetrahedra to construct a three dimensional framework. The chains alternate direction between [001] and [011]. This framework forms channels along the polar axis with potassium ions (K^+) located at the structural voids. Each of the TiO_6 groups contain a short Ti-O bond (1.7 Å) and a long Ti-O bond (2.1 Å)[12]. This difference in the Ti-O bond lengths makes the TiO_6 octahedra highly distorted and induces a net c-directed polarization. Figure 3.1 shows the KTP structure.

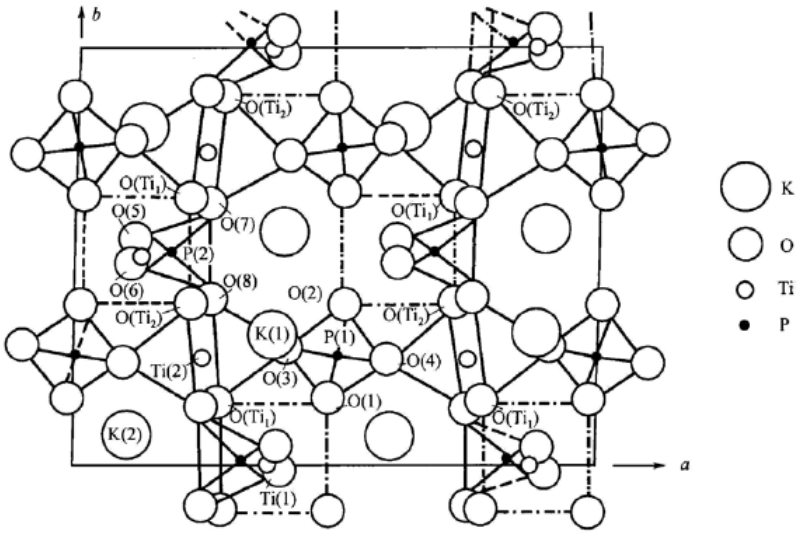

Figure 3.1[13] Projection of the KTP crystal along the (001) direction

KTP crystal morphology is shown in figure 3.2. The morphology consists of (100) planes, of the (201) and (011) series of planes that form relatively sharp caps along the c polar axis, and of the (011) and (110) series of planes that form shallower caps

along the b axis. Other high order planes can be present, but these usually form smaller faces.

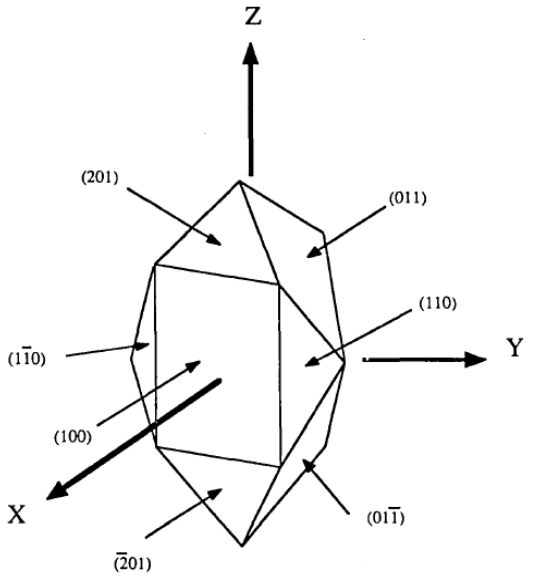

Figure 3.2[14] Natural KTP crystal morphology

3.3 Crystal Growth

KTP decompossess on melting around 1150° C. This makes melt-growth methods, such as the Czochraski method, improbable for KTP growth. Instead, crystals from the KTP family are grown from either the hydrothermal or flux methods.

3.3.1 Hydrothermal Method

The hydrothermal method consists of sealing the nutrient and seed crystal into a tube, inserting the tube into a high-pressure-high-temperature autoclave, and growing the crystals at constant pressure (1.4 to 1.724×10^8 Pa) and constant temperature (300° C to

600° C) with a fixed temperature gradient (~600° C at the nutrient end and ~550° C at the seed end). Dissolution of aqueous solvents at high temperature and pressures is carried out in the hot nutrient zone. The material is then transported via convection currents into the cooler growth zone where crystallization occurs. Hydrothermal growths take between 3 to 6 weeks to complete.

3.3.2 Flux Method

The flux technique is essentially a high-temperature solution growth process in which the KTP crystallizes out of a molten KTP/flux composition when cooled. Depending on the specific flux used, crystal growth can occur from 700° C to 1000° C. Common fluxes used are various potassium phosphates, with the K to P ratio from 1 to 3, tungstates and halides[14]. Flux growth is performed at atmospheric pressure in an accurately temperature controlled furnace to avoid crystal defects due to growth striations and flux inclusions. For KTP growth, crystallization starts in the supersaturated melt and continues while the temperature steadily decreases. Small crystals are made by spontaneous nucleation in the flux, while large crystals are grown from a seed inserted into the flux. There are two types of seeded growth. One is called submerged seed solution growth (SSSG) which gives a crystal with 14 growth sectors. The other one is called top seeded solution growth (TSSG) which gives a crystal with 10 growth sectors. The crystal site should be at the coolest spot in the flux to avoid secondary nucleation. Rotation of the crystal or the crucible prevents secondary nucleation by convection. Also, periodic reversal of the rotation avoids asymmetrical flow rates and flux in-homogeneity. A significant advantage to the flux method, over the hydrothermal

method, is that it operates at atmospheric pressures and therefore does not need sophisticated pressure equipment. Flux growths take between 10 days to 2 months depending on growth parameters.

3.4 Optical Properties

KTP has several nonlinear optical and thermal properties that make it ideal for second-order nonlinear applications and SHG. It has large nonlinear coefficients, low absorption and a wide acceptance angle. The large temperature bandwidth of KTP is particularly good for maintaining pulsed energy stability of the converted beam. Some of the nonlinear optical and thermal properties for KTP are listed in table 3.1.

Table 3.1[14] Nonlinear Optical and Thermal Properties of KTP

Property	Value
Nonlinear-optical coefficients (pm/V)	$d_{31} = 6.5$ $d_{32} = 5.0$ $d_{33} = 13.7$ $d_{24} = 7.6$ $d_{15} = 6.1$
Temperature bandwidth (°C cm)	25°
Angular bandwidth (mrad cm)[a]	15–68
Spectral bandwidth (Å cm)[a]	5.6
Walkoff (mrad)[a]	1
Temperature coefficients of refractive index ($°C^{-1}$)	$\Delta n_x = 1.1 \times 10^{-5}$ $\Delta n_y = 1.3 \times 10^{-5}$ $\Delta n_z = 1.6 \times 10^{-5}$
Transmission range (μm)	0.35–4.5
Optical absorption (%/cm)	<0.6 (at 1.064 μm) <2 (at 0.532 μm)
Thermal expansion coefficients ($°C^{-1}$)	$\alpha_1 = 11 \times 10^{-6}$ $\alpha_2 = 9 \times 10^{-6}$ $\alpha_3 = 0.6 \times 10^{-6}$
Thermal conductivity (W/cm°C)	$k_1 = 2.0 \times 10^{-2}$ $k_2 = 3.0 \times 10^{-2}$ $k_3 = 3.3 \times 10^{-2}$
Pyroelectric coefficient (nC/cm^2 °C)	7
Specific heat (cal/g °C)	0.174

The transmission of KTP (see figure 3.3) and its isomorphs has been measured by Hansson *et al*.[15] For KTP, the ultraviolet cut-off wavelength is 0.365 μm, and in the

infrared cut-off wavelength is 4.3 μm. The absorption in the high transmission window is less than 0.6 %/cm.

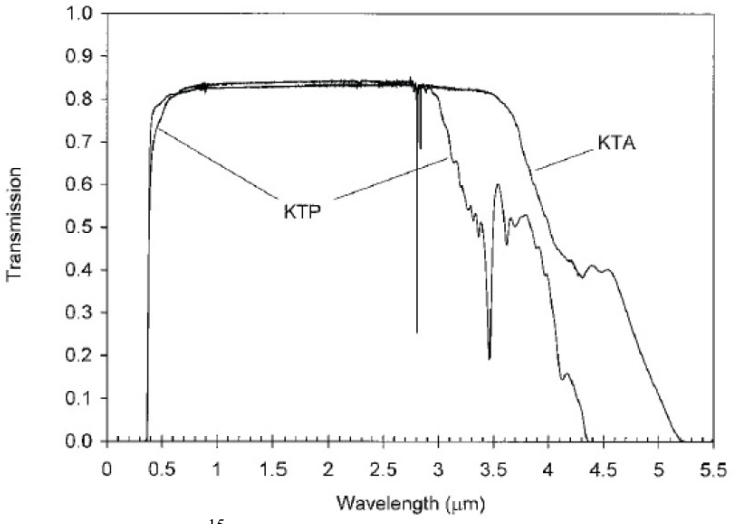

Figure 3.3[15] Transmission window for KTP and KTA

An important consideration when choosing a crystal for nonlinear optical applications is its resistance to optically induced damage. Photorefractive damage occurs when optically excited free carriers in the crystal get trapped outside the optical beam and set-up an internal field which distorts the beam via the electro-optical effect. KTP presents several orders of magnitude higher resistance to photorefraction than $LiNbO_3$, which has to be operated above 100° C, whereas KTP can be operated at room temperature.

3.5 Ionic Conductivity

The open nature of the KTP crystal, built up by the TiO_6 octahedra and the PO_4 tetrahedra, allows for the K^+ ions to diffuse readily along the polar axis via a vacancy hopping mechanism. The barrier for the hopping of the ions is about 0.3 eV at room temperature, which relates these crystals to one-dimensional superionic conductors[16]. Thereby, KTP gets a relative large and highly anisotropic ionic conductivity. The ionic conductivity along the polar axis is typically three to four times greater than that perpendicular to the polar axis.

The ionic conductivity of KTP varies depending on the crystal growth process and where on the wafer the crystal is taken from. Conductivity can vary as much as 4 orders of magnitude between crystals depending on the method and temperature with which they were grown[17]. The high conductivity of flux grown KTP is primarily attributed to the non-stoichiometry of the crystal, where K^+ vacancies are built into the structure, which are then available for ionic transport under an applied electric field. Hydrothermally grown crystals, on the other hand, have a higher degree of stoichiometry and therefore less conductive. Conductivity can also very considerably across a wafer, see figure 3.4. Doping KTP during the growth process can significantly reduce the ionic conductivity of the crystal by as much as 1.5 to 3 orders of magnitude[15]. However, some dopants occupy crystal lattice positions that inhibit domain reversal[15].

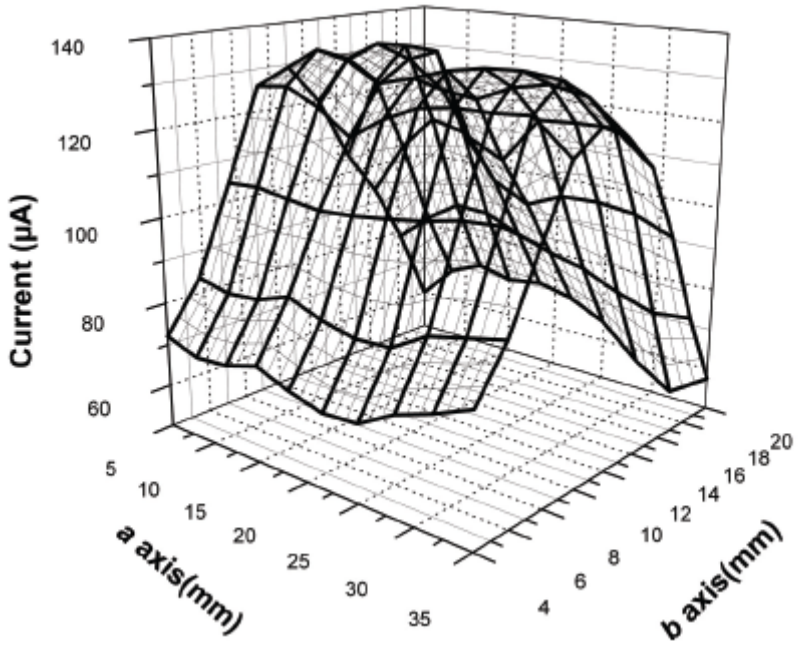

Figure 3.4[10]. Conductivity map of flux KTP showing the ionic-current variation over a wafer.

The coercive field in KTP is affected by high ionic conductivity. Flux grown KTP and its isomorphs are known to possess non-stiochiometric defects, which are M^+ ion and oxygen vacancies. The concentration of defects can vary depending on growth conditions. For example, in flux KTP grown at 970° C – 920° C the defect concentration is 500 – 800 ppm[18]. It is known that moving domain walls in ferroelectrics may interact with point non-stiochiometric defects such as vacancies and this can lead to an increase of the coercive field.

Previous work done by Urenski *et al*.[19] showed that lowering the temperature causes a reduction of K^+ ion mobility to a point where the ions are "frozen." The temperature behavior of dielectric relaxation in KTP as well as direct detection of the

charge carrier type form thermoelectric measurements confirm that at this freezing temperature the conductivity transitions from ionic to electronic conductivity.

For flux KTP Urenski found at 170 K a polarization switching time of 50 ms, considerably less than the dielectric relaxation time of 2 s at this temperature. Thus $\tau_{sw} << \tau$, and the depolarization field is compensated only by external charges flowing through the electrodes. At 300 K the switching time was found to be 10 ms compared to a dielectric relaxation time of approximately 10^{-6} s at this temperature. Here $\tau_{sw} >> \tau$ and the mobile K^+ ions may screen the depolarization field.

3.6 Domain geometry in KTP

Urenski *et al*[20]. showed that the domain growth geometry in KTP is dependent on whether the crystal is in the dielectric state or the superionic state. At 170 K, when KTP is in the dielectric state and the K^+ ions are frozen, domain nucleation forms at the positive electrode and grows toward the ground electrode with no domain wall broadening wider than the electrode. At 300 K, when KTP is in the superionic state where the K^+ ions have a high mobility, the nucleation of the domains can happen within the crystal bulk and the shape of the domains show broadening, with the overall end shape of the domain is narrower at the positive electrode than the ground. These effects can be seen in figure 3.5.

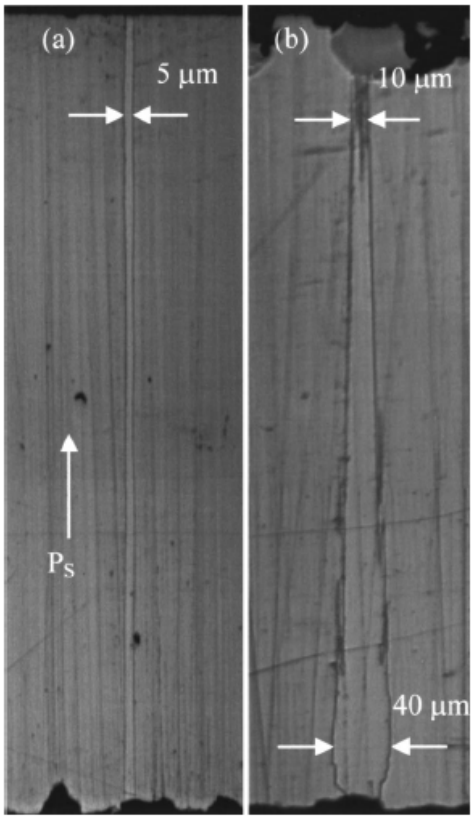

Figure 3.5[20]. View of the KTP sample polished at 45 degrees to the c-axis and etched after polarization reversal a) at 170 K and b) at 300 K

Chapter 4 Fatuzzo and Merz Work on Polarization Reversal in Ferroelectrics

4.1 Introduction

In the 1950's E. Fatuzzo and W. Merz studied polarization reversal in ferroelctrics namely barium titanate ($BaTiO_3$) and triglycine sulfate (TGS) [1,2]. During electrical poling current was measured indirectly via a resistor in series with the crystal. Square pulses of varying applied fields were used. This measurement is referred to as the Merz method in the literature. Figure 4.1 shows the characteristic current versus time curve observed by Fatuzzo and Merz in their studies on ferroelectrics.

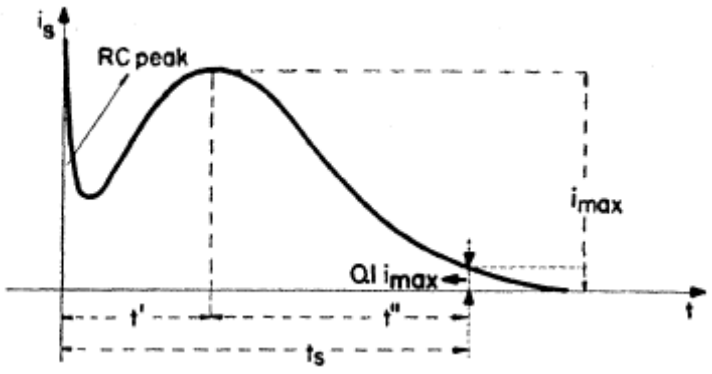

Figure 4.1[2] Characteristic switching pulse observed by Fatuzzo and Merz in their TGS study

Figure 4.1 shows the switching time (t_s), maximum switching current (i_{max}), and the switching charge (Q_s). The time taken for a reversal of polarization is known as the switching time. F&M define the switching time as the time from the application of the field to when the switching current falls to 90% of its maximum. The same convention

for switching time is used for the switching time data taken in this thesis. The maximum switching current is the peak current seen during the poling. The switching charge may be calculated by integrating the current over time. The derivation of switching time and maximum switching current by Fatuzzo and Merz are described below.

4.2 Switching time

Optical and electrical pulsing experiments performed by F&M showed that the poling process consists of two steps: nucleation of domains at the crystal surface and domain growth through the crystal (both forward and sideways). Figure 4.2 shows this process.

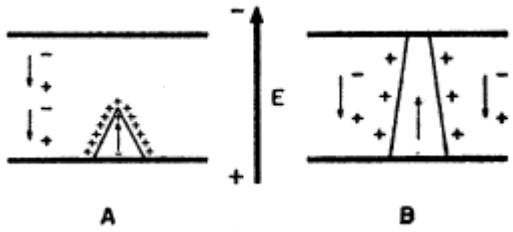

Figure 4.2[ref]. Domain growth process in a ferroelectric. A is nucleation, B is domain growth.

Nucleation of domains is attributed to a statistical process where domain growth is governed by a type of viscous drag. Each of these processes has a specific time association; t_n for nucleation time and t_d for domain growth time. The total switching time can therefore be approximated as the sum

$$t_s \cong t_n + t_d . \tag{4.1}$$

The expression for the nucleation time is found in the following manner. Assuming the nucleation of new domains is a statistical process then at low fields the probability of new domain formation will depend exponentially on the applied field as

$$p_n = p_o e^{-\alpha / E}, \tag{4.2}$$

and the inverse of the nucleation time can then be expressed as having an exponential dependence on the applied field as

$$\frac{1}{t_n} = \frac{1}{t_o} e^{-\alpha / E}. \tag{4.3}$$

In equations 4.2 and 4.3 p_o, t_o, and α are constants. The constant α is a temperature dependent fitting parameter representing an activation field related to the coercive field of the ferroelectric. Roughly $\alpha = 4E_c$ and therefore α may be used as a way to estimate the coercive field.

The expression for the domain wall growth time is found in the following way. The velocity of the domain wall growth can be expressed as

$$v = \frac{d}{t_d} = \mu E = \frac{\mu V}{d}. \tag{4.4}$$

Here d is the forward distance the domain wall moves and μ is the mobility of the domain wall. The inverse of the domain wall growth time may then be expressed as

$$\frac{1}{t_d} = \frac{\mu E}{d}. \tag{4.5}$$

Assuming the mobility is not field dependent, the ratio μ/d may be expressed as a constant, k, and the inverse of the domain wall growth time at high fields may be shown to have a linear relationship with the electric field as

$$\frac{1}{t_d} = kE. \tag{4.6}$$

Since $1/t_s = 1/(t_n+t_d)$, it is easy to see that t_s is governed by the larger of the two in the denominator. At low fields the rate of nucleation is low and $t_n >> t_d$, therefore the switching time is governed by the rate of nucleation and the inverse switching time may be expressed as

$$\frac{1}{t_s} = \frac{1}{t_o} e^{-\alpha / E}. \tag{4.7}$$

At high fields the rate of nucleation is large and $t_n << t_d$, therefore the switching time is governed by t_d and the inverse switching time may be expressed as

$$\frac{1}{t_s} = kE\,. \tag{4.8}$$

With the appropriate choice of the constants k, t_o and α Fatuzzo and Merz were able to fit their low field switching time data to equation 4.7 and their higher field data to equation 4.8 (see figure 4.3 below).

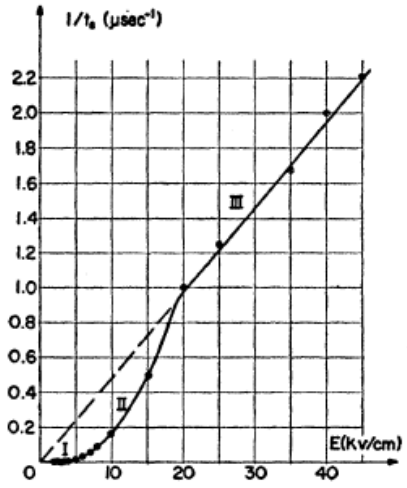

Figure 4.3 [2] Reciprocal switching time versus applied field for TGS

Figure 4.3 shows three regions (I, II, III). The regions are divided as follows: I is the low field region, II is the intermediate field region, and III the high field region. Equation 4.7 applies to region I and equation 4.8 applies to region III. Table 1, below, summarizes the results of the switching time experiments on TGS.

Table 4.1 [2] Properties of t_d and t_n

Low fields	Intermediate fields	High fields
$t_d \ll t_n$ $t_s \cong t_n = t_0 \exp(\alpha/E)$	$t_d \cong t_n$	$t_d \gg t_n$ $t_s \cong t_d = (KE)^{-1}$

Fatuzzo and Merz have the nucleation time and domain growth time approximately equal in the intermediate field range. No derivation of switching time dependence in the intermediate field range was done by Fatuzzo and Merz in their early work. However, Rosenman *et al*[21]. applied the Merz method to flux KTP at room temperature and came up with a power law fit, $t_s^{-1} = aE^n$ (with $n \approx 3.7$) for the intermediate field range in flux KTP. Rosenman poled KTP from1.5 kV/mm to 7 kV/mm and defined the three field regions as: low (1.5 kV/mm to 2.5 kV/mm), intermediate (2.5 kV/mm to 4.2 kV/mm), and high (greater than 4.2 kV/mm). Figure 4.4 below shows a plot of both maximum switching current and inverse switching time versus applied field for the KTP data found by Rosenman. Notice the proportionality in maximum switching current and inverse switching time with the field. With increasing applied field the maximum switching current should increase and the switching time decrease. Therefore the plots of maximum switching current and inverse switching time should look proportional under the same applied fields.

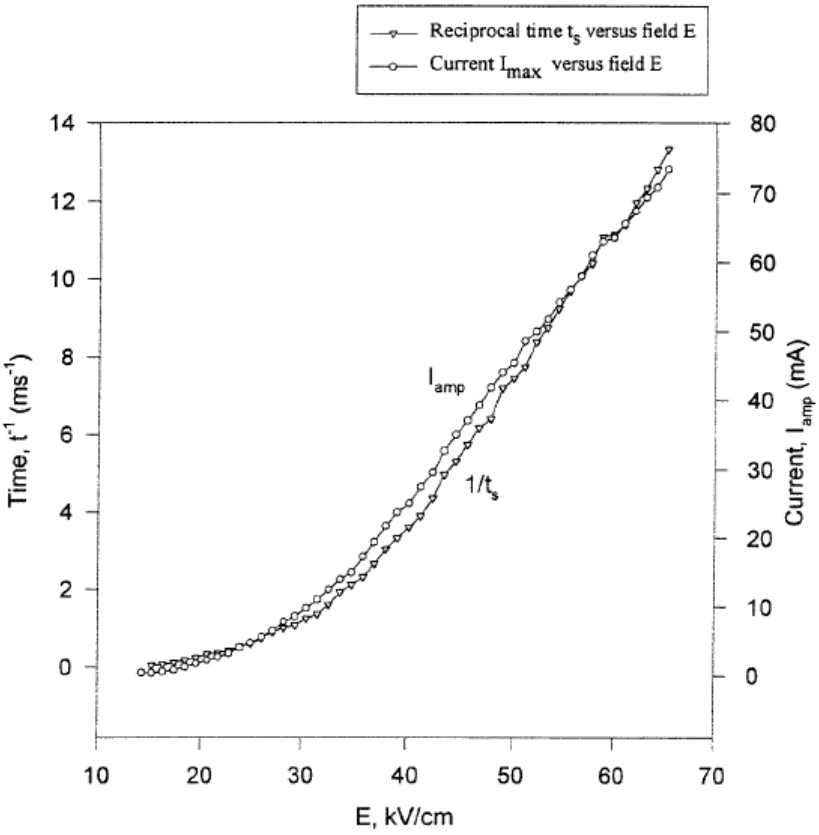

Figure 4.4[21]. Maximum switching cureent and inverse switching time versus applied field in flux KTP at room temperature.

4.3 Maximum switching current

A plot of the maximum switching current as measured by Merz in $BaTiO_3$ is shown below in figure 4.5. Merz was able to fit the maximum switching current data to the following exponential relation

$$i_{\max} \sim e^{-\alpha / E}. \tag{4.9}$$

The constant α in equation 4.9 is related to the constant found in equation 4.3.

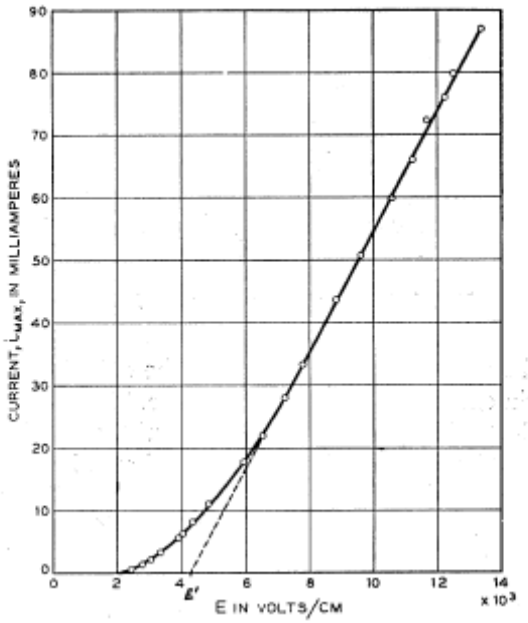

Figure 4.5[1] Maximum current vs. electric field as measured in barium titanate

At low fields the switching current is determined mainly by the number of nuclei created per unit time. The nucleation rate can be related to a Boltzmann like statistical function. Therefore the maximum switching current can be expressed as

$$i_{\max} \sim \frac{dn}{dt} \sim e^{\left(-\frac{\Delta F}{kT}\right)} \qquad (4.10).$$

where ΔF is the free energy of formation, k is Boltzmann's constant and T is the temperature. The free energy of formation of a nucleus with antiparallel polarization was given in chapter 2 in equation 2.3 as $\Delta F = -2EP_sV + \sigma_w A + \frac{1}{2}NP_s^2V$, where the first term is the energy of interaction between the P_s and the applied electric field E. The volume of the nucleus is V. The second term is the nucleus surface energy with A as the domain

wall area. The last term is the energy of the depolarizing field, caused by the divergence of polarization along the domain boundary. N is the depolarization factor.

Optical evidence gathered by Merz suggested that the geometry of the domain growth is that of a long cone or ellipsoid growing through the crystal. Assuming an ellipsoid geometry to be correct V, A, and N can be expressed as

$$V = a \cdot r^2 l\,, \tag{4.11}$$

$$A = brl\,, \tag{4.12}$$

$$N = \frac{cr^2}{l^2}\,, \tag{4.13}$$

where r is the radius of the base, l is the length of the nucleus, and a, b, and c are constants. By taking the derivative of equation 2.3 and setting it equal to zero the critical values for r and l can be found. They have the following relations

$$r^* \sim \frac{1}{EP} \tag{4.14}$$

and

$$l^* \sim \frac{1}{EP}\,. \tag{4.15}$$

Using equations 14 and 15 in equation 2.3 we get the following relation for the free energy of formation

$$\Delta F \sim \frac{1}{E^{5/2} P^{3/2}}\,. \tag{4.16}$$

Equation 4.16 may then be put into equation 4.10 for the rate of nucleation yielding

$$i_{\max} \sim \frac{dn}{dt} \sim e^{\left(-\frac{\Delta F}{kT}\right)} \sim e^{\left(-\frac{C}{E^{5/2}P^{3/2}kT}\right)}, \tag{4.17}$$

which is not the $e^{-1/E}$ dependence found experimentally.

The $e^{-1/E}$ dependence was derived by making the following assumptions. First assume that the depolarizing field can be neglected because the nucleus is very long and thin. Second, assume that the shape of the domain is that of a long flat dagger (see figure 4.6) with length l parallel to the applied field and a width and thickness where $t < w << l$.

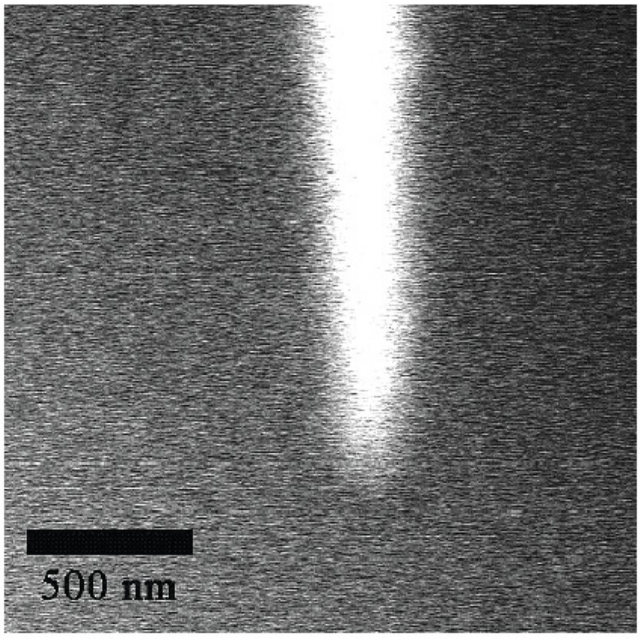

Figure 4.6[22]. Dagger like shape of domain growth in KTP

Now the formation of free energy can be written as

$$\Delta F = -2EPlwt + \sigma_w^{'}(wl + tl) + \sigma_w^{''}wt \tag{4.18}$$

and with $w > t$,

$$\Delta F = -2EPlwt + \sigma_w^{'}wl + \sigma_w^{''}wt\ . \tag{4.19}$$

Now the critical dimensions are found to be

$$t^* \sim \frac{\sigma_w^{'}}{EP} \tag{4.20}$$

and

$$l^* \sim \frac{\sigma_w^{''}}{EP} \tag{4.21}$$

giving

$$\Delta F \sim \frac{\sigma_w^{'}\sigma_w^{''}}{EP} \tag{4.22}$$

and thus

$$i_{\max} \sim \frac{dn}{dt} \sim \exp\left(-\frac{\sigma_w^{'}\sigma_w^{''}}{EPkT}\right), \tag{4.23}$$

which gives the $e^{-1/E}$ dependence found experimentally. Equations 4.20 and 4.21 and $t << l$ implying $\sigma_w^{''} >> \sigma_w^{'}$, that is the wall energy of the front wall is much larger than the energy of the side walls.

4.4 Switching charge

As mentioned before the switching charge can be calculated by integrationg the area under the switching pulse. The switching charge is related to the spontaneous polarization as

$$Q_s = 2P_s A = \int i dt\,, \tag{4.24}$$

where P_s is the spontaneous polarization and A is the electrode area. Therefore, the spontaneous polarization may be found by dividing the switching charge by twice the electrode area.

Chapter 5 Experiment

5.1 The samples

Two hydrothermaly grown samples from the same wafer and two flux grown samples from the same wafer were studied in this thesis. For proprietary reasons, the exact growth conditions for the samples cannot be reported. However, it can be said that the hydrothermal samples came from a low temperature process. The hydrothermal samples will be referred to as H1 and H2 and the flux grown samples will be referred to as F1 and F2. All samples were cut normal to the c-crystallographic axis and polished. Samples F2, H1 andH2 have the dimensions *10 mm (x-axis), 5 mm (y-axis), and 1 mm (z-axis)*. Sample F1 broke in half during processing for study and has the dimensions *5 mm (x-axis), 5 mm (y-axis), and 1 mm (z-axis).* Each sample had gold/chrome contacts applied to the top and bottom planes normal to the *c-axis* by metal sputtering. The chrome was applied with a thickness around 100 Å and the gold was applied on top of the chrome with a thickness of 1 μm. Figure 5.3 shows a hydrothermal sample with and without contacts. The flux samples looked identical.

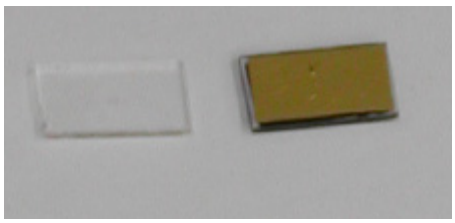

Figure 5.1. KTP sample, left side is without gold/chrome contacts, right side has gold /chrome contacts.

5.2 Apparatus

A schematic of the experimental apparatus can be seen in figure 5.1. A listing of the apparatus follows: a Windows PC with Visual Basic interface, a Wavetek model 275 function generator, a Trek model P0621 power supply, an Agilent Technologies MSO6104A oscilloscope, and a polarity switch. A high voltage switch was constructed out of a relay to reverse the polarity of the applied electric field during the experiments.

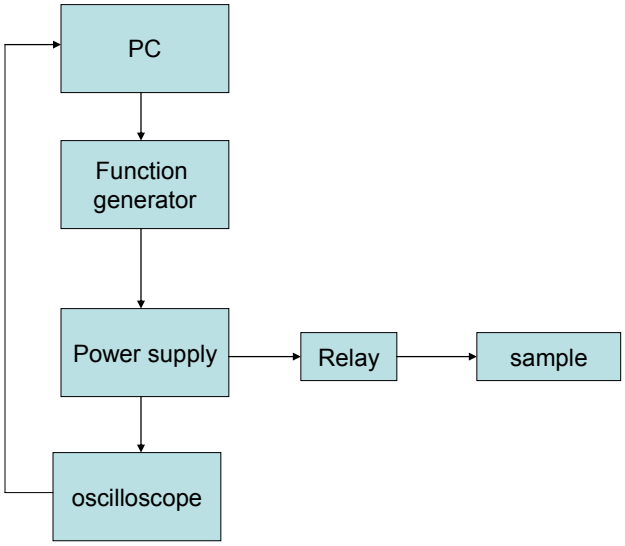

Figure 5.2. Schematic of experimental setup.

Gold wires were welded to the gold/chrome contacts and soldered to the poling apparatus electrodes. The samples were then submerged in a petri dish filled with silicone oil to prevent electrical arching from the top and bottom electrodes during application of the electric field, see fig. 5.4.

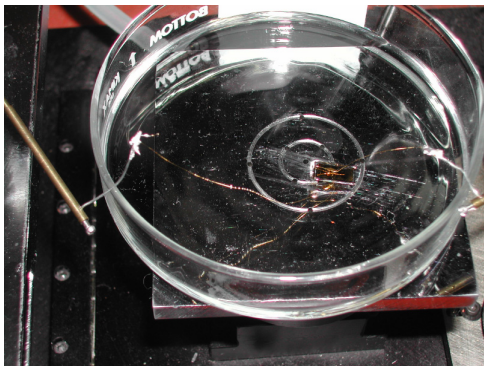

Figure 5.3. Metal contacted KTP sample submerged in perti dish full of silicone oil

5.3 Procedure

KTP exhibits an asymmetry in the magnitude of the maximum current for the same applied field from one polarity to the other along the polarization axis (c-axis). Each sample was then poled with an initial voltage of 3000V/mm with both positive and negative polarity. The sign of the polarity showing the largest maximum switching current under the 3000 V/mm pulses were designated “forward” and the other “reverse” (see figure 5.4). The samples were then poled from 1600 V/mm to 5000 V/mm in the forward direction with alternating 3000 V/mm reverse pulses up to 3000 V/mm where the reverse poling was then continued with eequal magnitude up to 5000 V/mm. Each voltage pulse was a square pulse of 1 second duration and a 5 ms ramp (see figures 5.5 and 5.6).

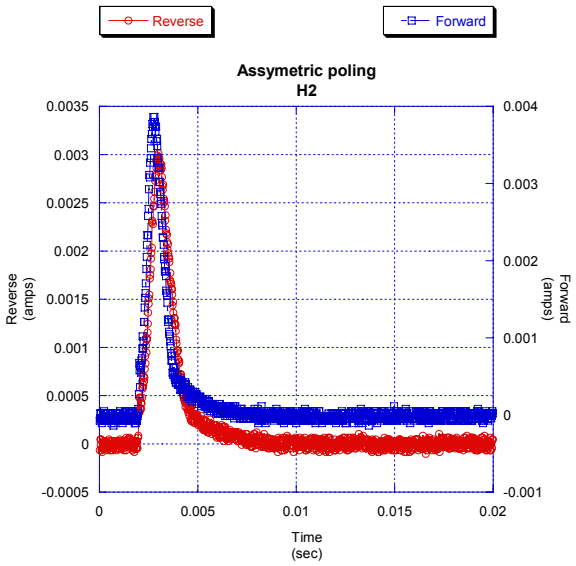

Figure 5.4. Asymmetric poling.

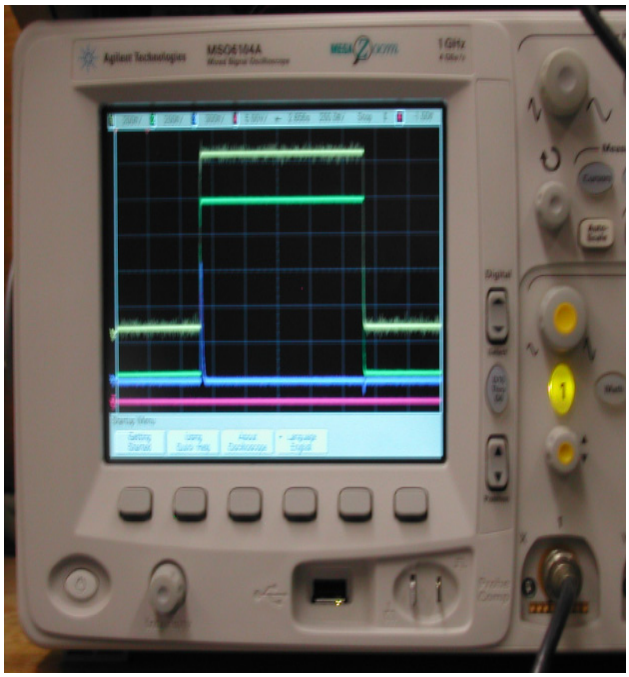

Figure 5.5. Square pulse applied to KTP during poling run

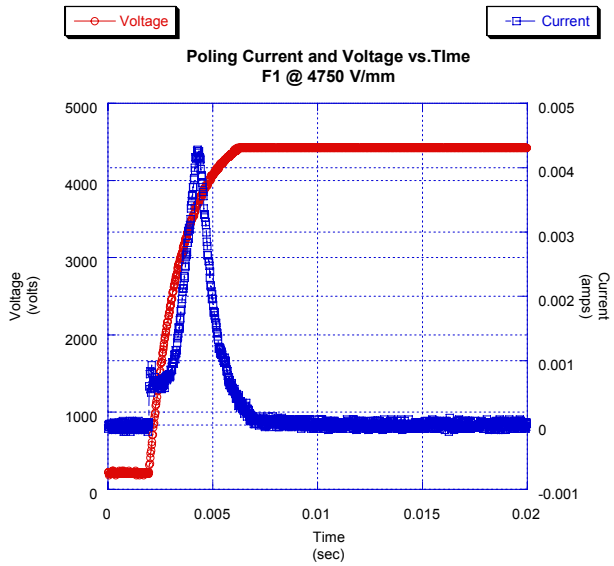

Figure 5.6. Poling current and voltage versus time

In order to ensure the poling system would measure expected voltages the output voltage of the power supply was measured across a voltage divider, two 1 MΩ resistors. A voltage of 3000V was applied and the oscilloscope showed roughly 1500 V across one of the resistors.

Schematics of the resistive load and capacitive load seen by the power supply are shown in figures 5.7 and 5.8, respectively. The resistance is almost entirely contained in the sample (~1 MΩ) and the capacitance comes mostly from the coaxial cables connecting the equipment (142 pF).

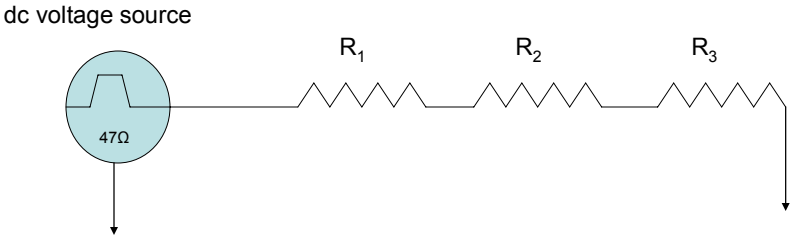

R_1 – cable (5 ft @ 100mΩ/ft = 500mΩ

R_2 – relay (20mΩ)

R_3 – sample (1MΩ)

$R_3 >> (R_2+R_1)$

Figure 5.7. Resistive load seen by power supply

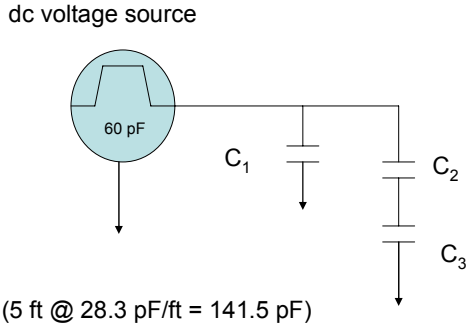

C_1 – cables (5 ft @ 28.3 pF/ft = 141.5 pF)

C_2 – relay box (2.5 pF)

C_3 – sample (C = εA / d = 10 pF)

$C_{load} = C1+(1/C2+1/C3)^{-1} = 143.5$ pF

Figure 5.8. Capacitive load seen by power supply

Using the capacitive load equation from the power supply manual the current needed to drive the capacitive load of the poling circuit (~2 mA) was found to be well below the maximum value of the power supply (40 mA). The slew rate needed for the experiment

(~1 V/μs) was found to be well below that of the maximum slew rate of the power supply (350 V/μs). The calculations are shown below.

The equation for driving a capacitive load is taken from the Trek model P0621 power supply manual and is

$$i = (C_{load} + 60\,pF)dV / dt \tag{5.1}$$

where i is the peak current needed from the amplifier, C_{load} is the load capacitance, $60\ pF$ is the internal capacitance of the amplifier, dV is the peak value of the square wave, and dt is the rise time required. Therefore, with the maximum values ($C_{load} = 144\ pF$, $dV = 5000V$, $dt = 5\ ms$) we get $i = (204\ pF)*(5000\ V)/(5\ ms) = .204\ mA$. The maximum slew rate needed for the experiment was found to be $5000\ V / 5\ ms = 500000\ V/s = 1.0\ V/\mu s$.

Chapter 6 Results and Analysis

6.1 Introduction

KaleidaGraph™ data analysis and graphing software was used to fit the KTP data. At low and high fields the inverse switching time versus applied field was fit to the Fatuzzo and Merz exponential and linear models, respectively. For the intermediate fields, the inverse switching time versus applied field data was fit to the power relation found by Rosenman for Flux KTP. Switching charge for the samples was calculated using equation 4.24. The flux samples will be presented first followed by the hydrothermal samples. The format will be presentation of data followed by a summary and discussion.

6.2 Flux Samples

F1 was damaged during processing for measurement. The sample cracked in half during the welding of gold wires to the gold/chrome contacts. Data from 1600 V/mm – 3000 V/mm was taken before the damage and will be compared to the 1600 V/mm – 5000 V/mm data taken after the damage. Plots of inverse switching time and maximum switching current together versus the applied electric field for both flux samples are shown in figures 6.1 - 6.3. Fitting of the low, intermediate and high field regions are shown in figures 6.4 – 6.10 and table 6.1 summarizes the fitting results. Switching charge data for both flux samples are shown in figures 6.9 - 6.11 and summarized in table 6.2.

6.2.1 Maximum switching current and inverse switching time data

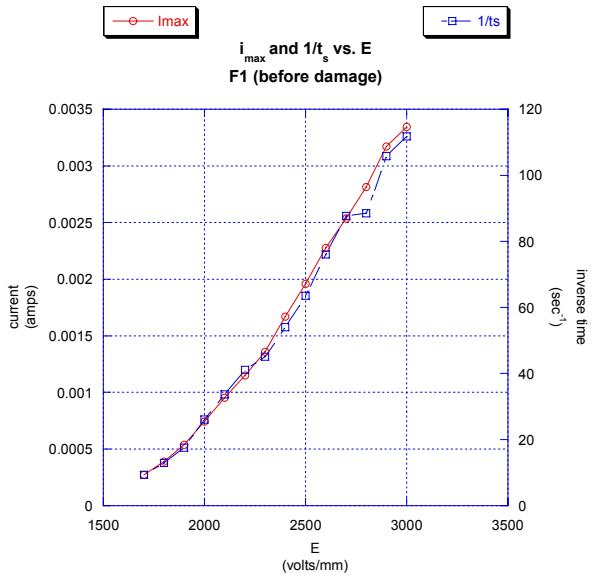

Figure 6.1. Inverse switching time and maximum switching current versus E, F1 (before damage).

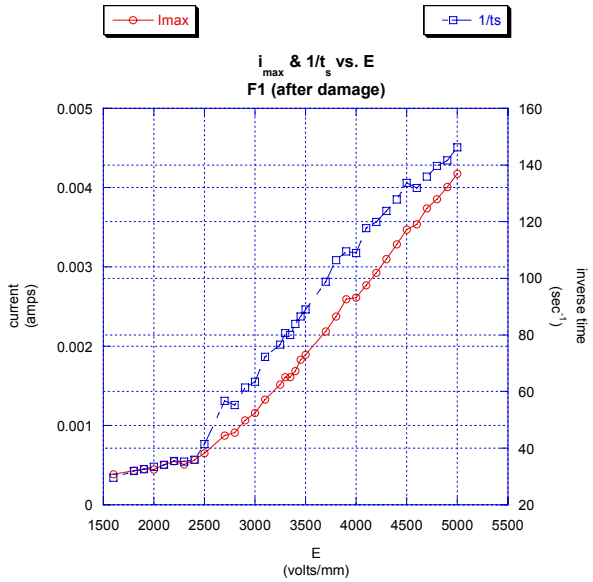

Figure 6.2. Inverse switching time and maximum switching current versus E-field, F1 (after damage).

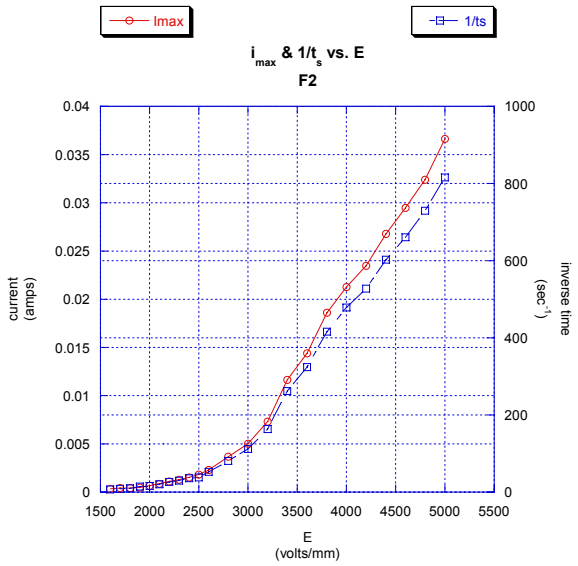

Figure 6.3. Inverse switching time versus E-field, F2.

6.2.2 Low field fits

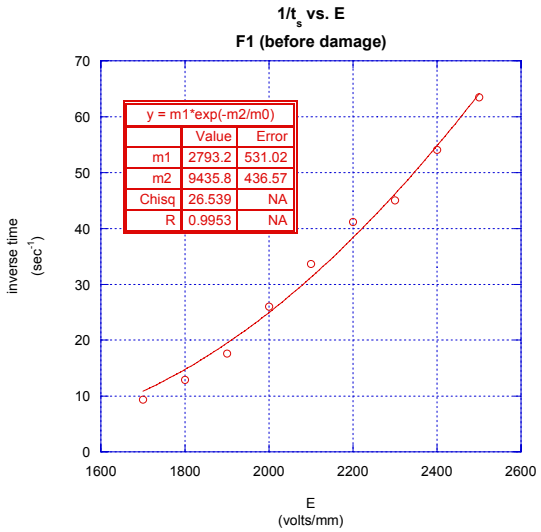

Figure 6.4. Inverse switching time versus E-field (low field), F1 (before damage).

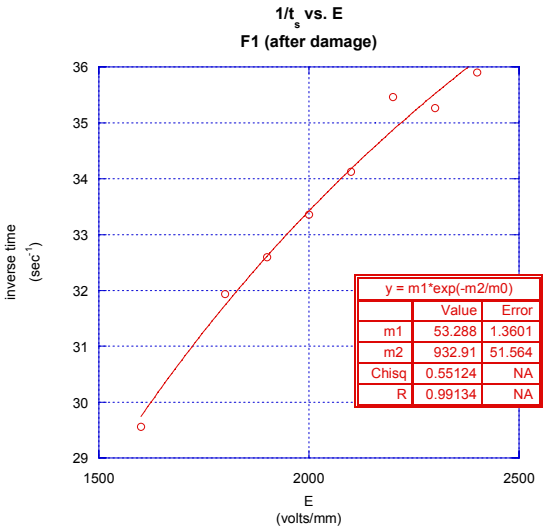

Figure 6.5. Inverse switching time versus E-field (low field), F1 (after damage).

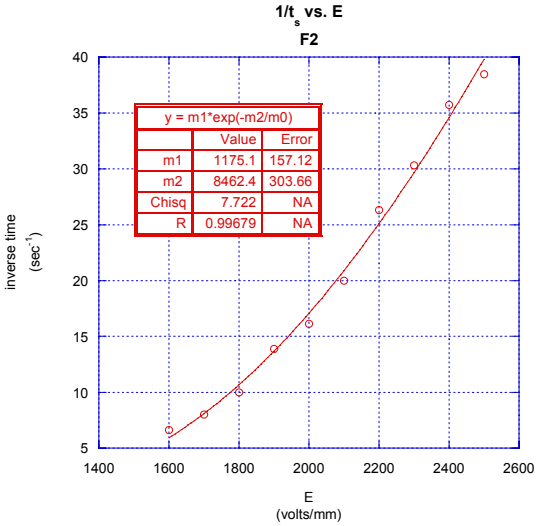

Figure 6.6. Inverse switching time versus E-field (low field), F2.

6.2.3 Intermediate field fits

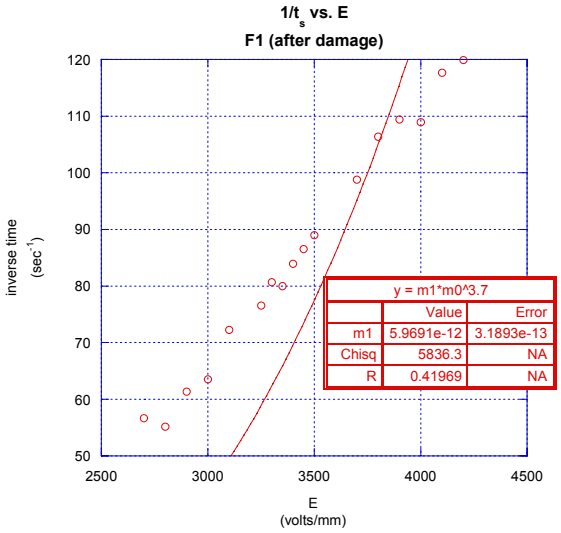

Figure 6.7. Inverse switching time versus E (intermediate field), F1.

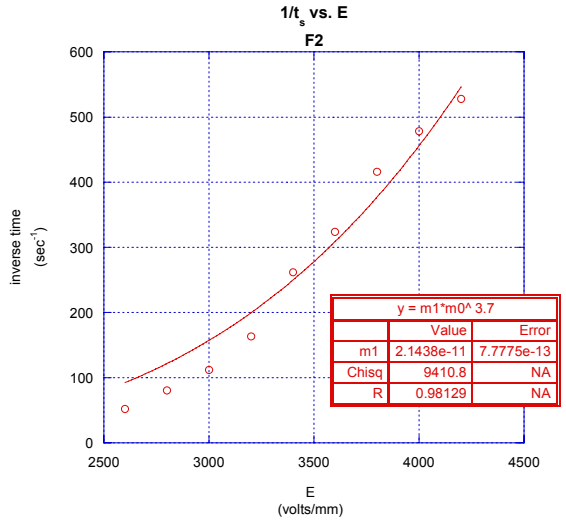

Figure 6.8. Inverse switching time versus E-field (intermediate field), F2.

6.2.4 High field fits

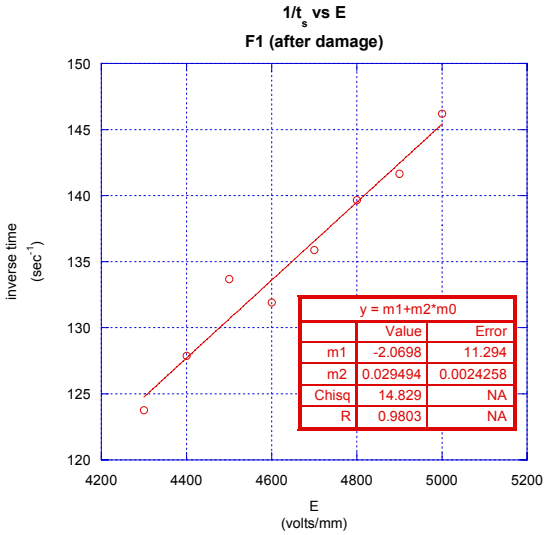

Figure 6.9. Inverse switching time versus E (high field), F1.

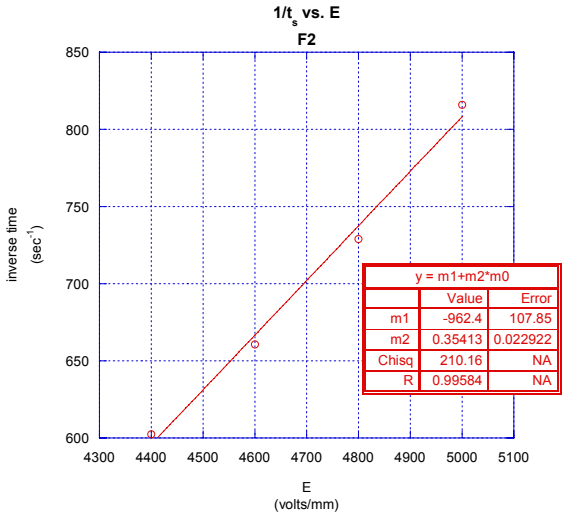

Figure 6.10. Inverse switching time versus E (high field) , F2.

6.2.5 Switching charge data

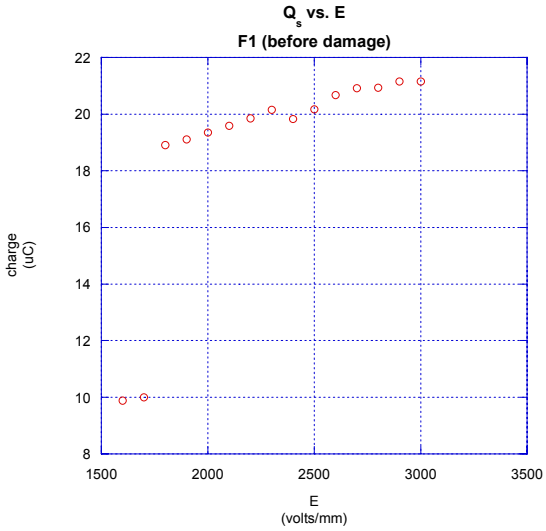

Figure 6.11. Switching charge versus E-field, F1.

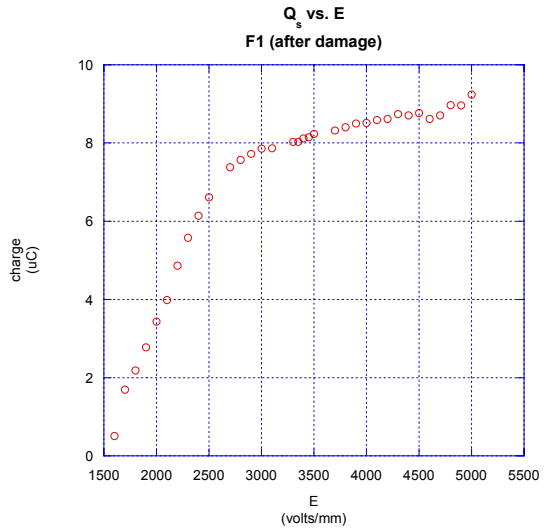

Figure 6.12. Switching charge versus E-field, F1.

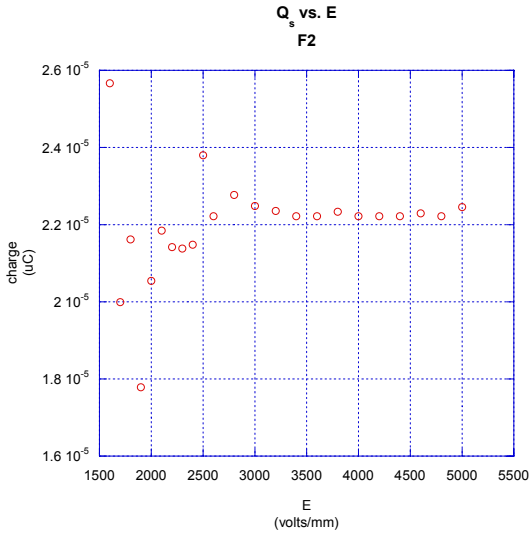

Figure 6.13. Switching charge versus E-field , F2.

6.2.6 Data summary and discussion

The low field data for F1 before damage and the high field data for F1 after damage appear to broadly follow the Fatuzzo and Merz model. The low and high field data for F2 appear to also follow the Faztuzzo and Merz model and the intermediate field data appears to follow the power relation found by Rosenman. Comparing the low field data for F1 before the damage and the low field data for F2 one is able to calculate a value for the coercive field close to the reported value (2.1 kV/mm)[10]. After the damage, F1 yields a coercive field value almost 1/10th that of the reported value.

Table 6.1. Summary of high, intermediate, and low field fits for F1 and F2

Sample	low fields (1.6 kV/mm < E < 2.5 kV/mm)	intermediate fields (2.6 kV/mm < E < 4.2 kV/mm)	high fields (E >4.2 kV/mm)
Fatuzzo, Merz and Rosenman	$t_s^{-1} = t_o^{-1} e^{-\alpha / E}$ $E_c \approx \alpha / 4$	$t_s^{-1} = aE^n, n \approx 3.7$	$t_s^{-1} = kE$
F1 (before damage)	$t_s^{-1} = 2793 e^{-9436/E}$ $\Delta t_o^{-1} = \pm 531$ $\Delta\alpha = \pm 436$ $E_c = 2359$ V/mm $\Delta E_c = \pm 109$ V/mm	N/A	N/A
F1 (after damage)	$t_s^{-1} = 53 e^{-933/E}$ $\Delta t_o^{-1} = \pm 1$ $\Delta\alpha = \pm 52$ $E_c = 233$ V/mm $\Delta E_c = \pm 13$ V/mm	$t_s^{-1} = 5.97 \times 10^{-12} E^{3.7}$ $\Delta a = \pm 3.19 \times 10^{-13}$	$t_s^{-1} = 0.029E$ $\Delta k = \pm 0.002$
F2	$t_s^{-1} = 1175 e^{-8462/E}$ $\Delta t_o^{-1} = \pm 157$ $\Delta\alpha = \pm 304$ $E_c = 2115$ V/mm $\Delta E_c = \pm 76$ V/mm	$t_s^{-1} = 2.14 \times 10^{-11} E^{3.7}$ $\Delta a = \pm 0.08 \times 10^{-11}$	$t_s^{-1} = 0.35E$ $\Delta k = \pm 0.02$

When comparing the low field data for F1 before and after the damage it can be seen that after the damage the there was a reduction in both the maximum switching current and switching time. Stress induced defects may have been introduced when F1 was damaged. These defects could have caused regions in the sample where some of the domains became frozen in a particular polarization orientation reducing the amount of sites available for domain nucleation and growth and resulting in a decrease of the switching current and increase of the switching time. This might also explain why the intermediate field fit for F1 is not very good. It may be that the defects caused by the damage to F1 were overcome at higher fields, but not at low or intermediate fields. The difference in the maximum switching current and switching time between F1 and F2 at low or high fields may be due to large variations in conductivity over the wafer from which the samples were taken (see figure 3.4).

Table 6.2. Switching charge versus applied field data for F1 and F2

Sample	Q_s statistics and P_s calculations • δ – standard deviation in Q_s • $P_s = Q_s / (2A)$ • A – area of electrode
F1 (before damage)	1800 – 3000 V/mm, Q_s = (20.14, δ = 0.78) μC, A = 0.5cm^2 @ 3000 V/mm, Q_s = 21.16 μC , P_s = 21.16 μC/cm^2
F1 (after damage)	3000 – 5000 V/mm, Q_s = (8.48, δ = 0.38) μC, A = 0.25cm^2 @ 3000 V/mm, Q_s = 7.86 μC , P_s = 15.7 μC/cm^2 @ 5000 V/mm, Q_s =9.24 μC , P_s =18.5 μC/cm^2
F2	2100 – 5000 V/mm, Q_s = (22.23, δ = 0.54) μC, A = 0.5cm^2 @ 3000 V/mm, Q_s = 22.5 μC , P_s = 22.5 μC/cm^2 @ 5000 V/mm, Q_s = 22.5 μC , P_s = 22.5 μC/cm^2

Spontaneous polarization calculations are listed above in table 6.2. At 3000 V/mm there was a noticeable reduction in the spontaneous polarization for F1 after damage compared

to before the damage. This seemed to recover slightly at higher fields. At 5000 V/mm both F1 and F2 data gave spontaneous polarizations close to the reported value (20.1 μC/cm^2)[21]. When looking at the charge data for F2 (figure 6.13) after 2100 V/mm the switching charge was 22.23 μC, with a standard deviation of 0.54 μC. The switching charge data for F1 before damage gives a switching charge of 20.14 μC, with a standard deviation of 0.78 μC over a field range of 1800 V/mm – 3000 V/mm. After the damage the sample was half the size as before (*5x5x1* vs. *5x10x1*) mm. After the damage the switching charge did not seem to be stable until after 3000 V/mm. This may be evidence of the damage causing an increase in the coercive field.

6.3 Hydrothermal samples

Plots of inverse switching time and maximum switching current together versus the applied electric field for both hydrothermal samples are shown in figures 6.11 and 6.12. Fitting of the low and high field regions are shown in figures 6.13 – 6.16 and table 6.3 summarizes the fitting results. Switching charge data for both hydrothermal samples are shown in figures 6.17 and 6.18 and summarized in table 6.4. Discussion follows both tables.

6.3.1 Maximum switching current and inverse switching time data

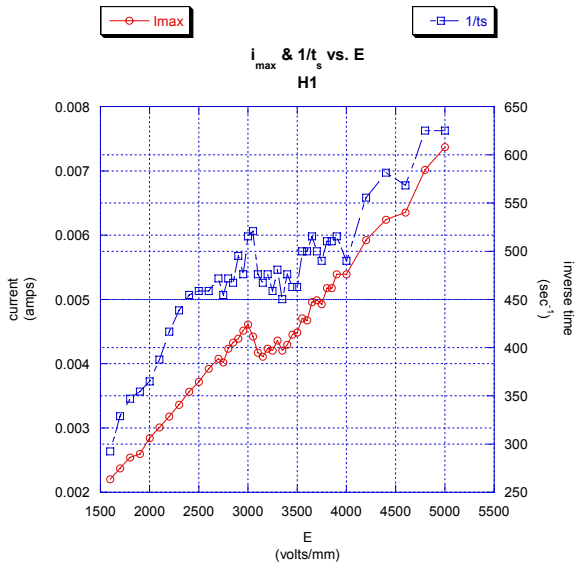

Figure 6.14. Maximum switching current and inverse switching time versus E-field, H1.

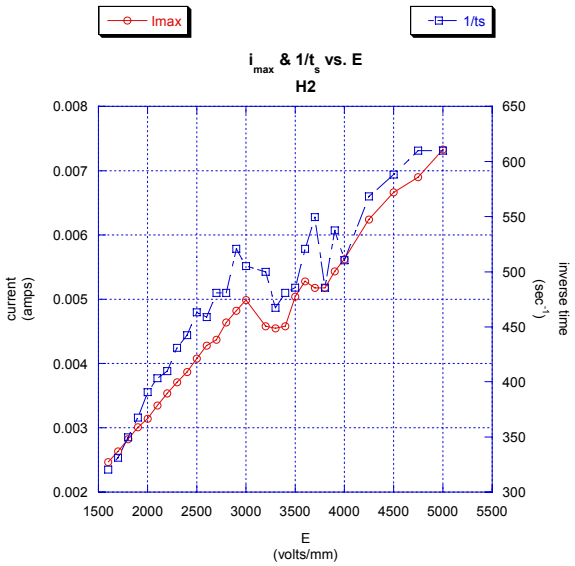

Figure 6.15. Maximum switching current and inverse switching time versus E-field, H2.

6.3.2 Low field fits

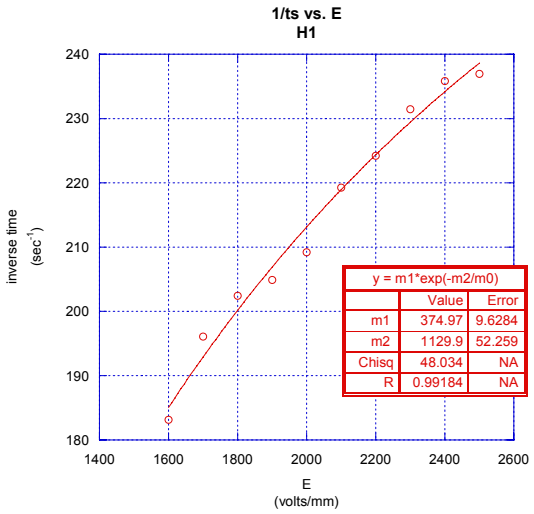

Figure 6.16. Inverse switching time versus E-field (low field), H1.

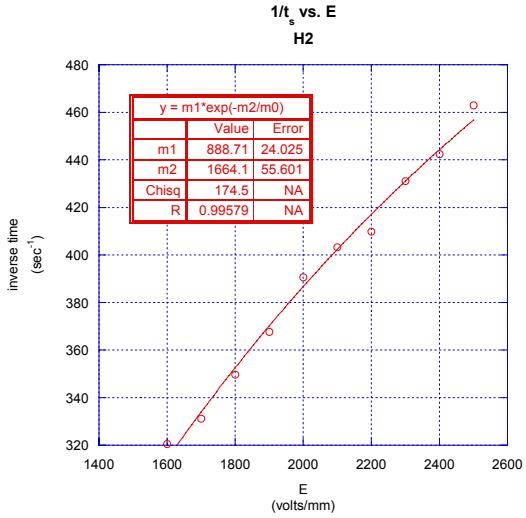

Figure 6.17. Inverse switching time versus E-field (low field), H2.

6.3.3 High field fits

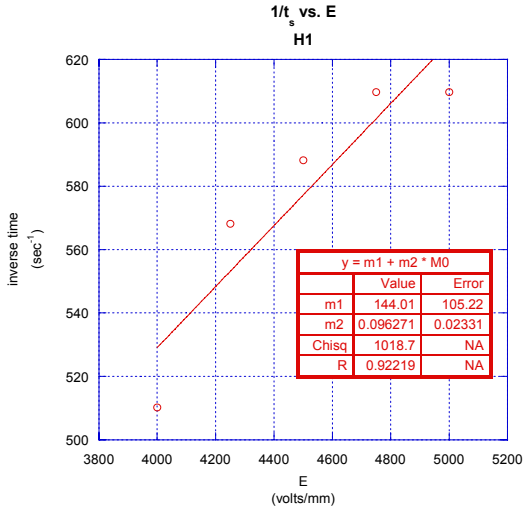

Figure 6.18. Inverse switching time versus E-field (high field), H1.

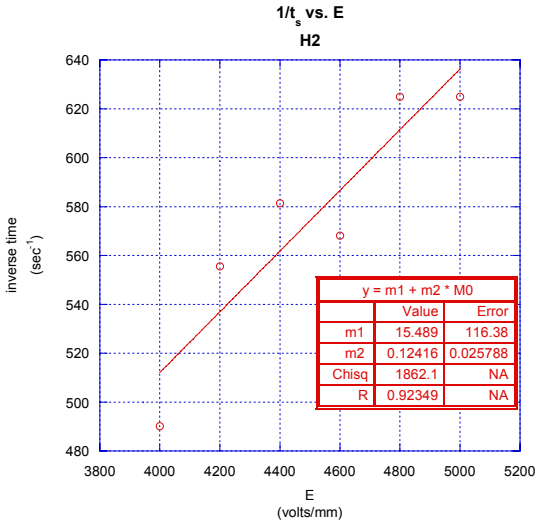

Figure 6.19. Inverse switching time versus E-field (high field), H2.

6.3.4 Switching charge data

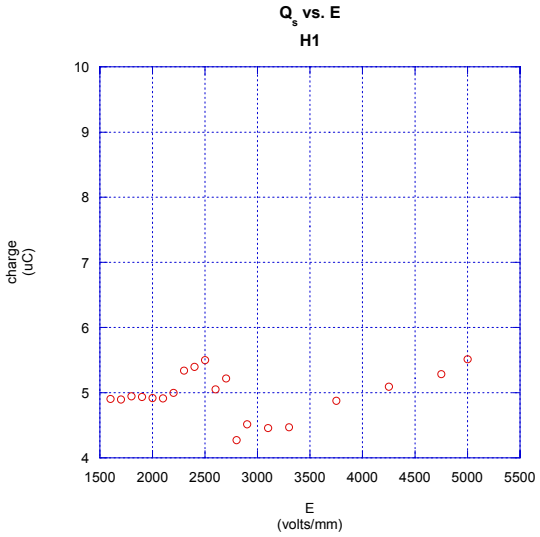

Figure 6.20. Switching charge versus E-field, H1.

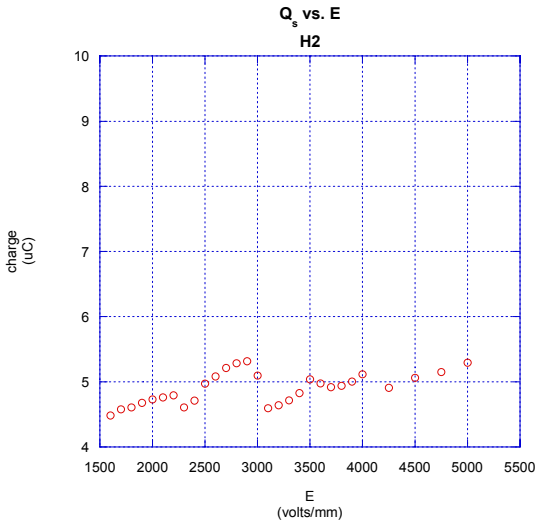

Figure 6.21 Switching charge versus E-field, H2.

6.3.5 Summary data and discussion

Table 6.3 shows the summary of the inverse switching time data for the hydrothermal samples. Only low field and high field regions were done due to the odd behavior of the flux samples in the intermediate region (see figures 6.14 and 6.15). The low field data for both samples seem to broadly follow the fatuzzo and Merz model. That is, the fits look plausible, the errors in the fits are low, and the R values (correlation confidents) are close to 1. However, the shapes of the fits have a different curvature compared to those of the flux fits in the low field region. The high field fits are not quite as good. They have large errors and low R values. As mentioned previously the flux data showed some odd behavior in the intermediate field range. From 3000 V/mm to 4000 V/mm both hydrothermal samples showed regions where the maximum switching current decreases while the switching time increases. This would suggest retardation in the domain nucleation and/or growth.

Table 6.3. Switching time fits for H1 and H2

Sample	low fields (1.6 kV/mm < E < 2.5 kV/mm)	high fields (E >4.2 kV/mm)
Fatuzzo, Merz and Rosenman	$t_s^{-1} = t_o^{-1} e^{-\alpha / E}$ $E_c \approx \alpha / 4$	$t_s^{-1} = kE$
H1	$t_s^{-1} = 375 e^{-1130 / E}$ $\Delta t_o^{-1} = \pm 10$ $\Delta \alpha = \pm 52$ $E_c = 283$ V/mm $\Delta E_c = \pm 13$ V/mm	$t_s^{-1} = 0.096 E$ $\Delta k = \pm 0.023$
H2	$t_s^{-1} = 889 e^{-1664 / E}$ $\Delta t_o^{-1} = \pm 24$ $\Delta \alpha = \pm 56$ $E_c = 416$ V/mm $\Delta E_c = \pm 14$ V/mm	$t_s^{-1} = 0.124 E$ $\Delta k = \pm 0.026$

Looking at the charge data for the hydrothermal samples (table 6.4) gives us some clues for explaining the behavior of the hydrothermal samples. First we notice that the hydrothermal samples yield switching charges and spontaneous polarizations about 1/4th that of the flux samples. This could be due to crystal fatigue. The fatigue could be caused by the application of the welding pulse to the sample and or the repeated poling of the samples prior to use in this study. All the samples were poled at least 50 times with fields up to 3000 V/mm in other experiments before being used for this study. The welding pulses and/or the cycling of previous poling could have induced ferroelectric fatigue in the samples which is known to lower the spontaneous polarization. Also, the maximum switching current for both samples was around 7.25 mA at 5000 V/mm which is a relatively high current for hydrothermal KTP. This could be due to an increase in the

coercive field which is another indication of ferroelectric fatigue. Something else to point out is that at intermediate to higher fields domain growth through the sample accounts for more of the switching time than at lower fields. It is then plausible to expect that forward and sidewise growth of domains could be slowed down as the domain walls encounter these defects.

Table 6.4. Switching charge versus applied field data for H1 and H2

Sample	Q_s statistics and P_s calculations • δ – standard deviation in Q_s • $P_s = Q_s / (2A)$ • A – area of electrode
H1	(1600 – 5000) V/mm, Q_s = (4.98, δ = 0.35) μC, A = 0.5cm^2 @ 2500 V/mm, Q_s = 5.45 μC , P_s = 5.45 μC/cm^2 @ 5000 V/mm, Q_s = 5.52 μC , P_s = 5.52 μC/cm^2
H2	(1600 – 5000) V/mm, Q_s = (4.90, δ = 0.24) μC, A = 0.5cm^2 @ 2500 V/mm, Q_s = 4.97 μC , P_s = 4.97 μC/cm^2 @ 5000 V/mm, Q_s = 5.29 μC , P_s = 5.29 μC/cm^2

Chapter 7 Conclusion

7.1 Summary

The data from the undamaged flux samples seems to broadly follow the Fatuzzo and Merz model at low and high fields and Rosenaman's intermediate field data. Also, the data from the undamaged flux samples seems consistent with that of Rosenman. Namely the maximum switching current and inverse switching time data is comparable to that of Rosenman's flux data (see figures 4.4, 6.1, and 6.3). Differences in maximum switching current and inverse switching time between the flux samples used in this thesis and those of Rosenman could be due to where the sample is taken form on the wafer as well as the parameters specific to each flux growth.

The low field data from the hydrothermal samples appears to follow the Fatuzzo and Merz model, but it is suspected that the hydrothermal samples are suffering from ferroelectric fatigue, especially due to their low spontaneous polarization calculations. If fatigue is responsible for the odd behavior in the hydrothermal samples adherence to the Fatuzzo and Merz model may not be possible.

The flux samples had the same history as that of the hydrothermal samples in that they were cycled at least 50 times at fields up to 3000 V/mm before use in this study. However, they did not appear to suffer from fatigue. However, there is evidence of defect introduction in F1 due to the sample cracking in half as seen by the decrease in both the maximum switching current and the switching time.

This study used square pulses with 5 ms ramps. This resulted in a non-uniform field on the samples during the poling runs (see figure 5.6). This did not seem to affect the flux samples, but it can not be said to have not affected the hydrothermal samples considering there odd behavior.

When looking at the maximum currents obtained for all the samples it would appear the initial calculation of the capacitive load was off considerably. This extra capacitance is most likely due to the gold/chrome contacts which were not included in the original calculation. However, the data from the flux samples appears close to that of Rosenman so as far as a comparative study there is not much worry. The hydrothermal samples may have been affected.

7.2 Future Work

It would seem that flux KTP broadly follows the Fatuzzo and Merz model and therefore further study of flux KTP as to its adherence to Fatuzzo and Merz may not be necessary. What may be of interest is studying the polarization reversal of flux KTP under known growth conditions to see what conditions might optimize flux KTP for room temperature poling.

As for hydrothermal KTP is would be of interest to see whether other hydrothermal KTP growths exhibit the same odd intermediate field behavior seen in the hydrothermal samples studied in this thesis. These experiments should be done using step pulses as opposed to square pulses to see if there is a difference in the results. Also,

the use of both metal and liquid contacts should be used and results compared to see what effects if any the metal has on the poling dynamics.

References

1. W.J Merz, Phy. Rev. 95, 690 (1954)
2. E. Fatuzzu and W. J. Merz, Physical Review 116, 1 (1959)
3. Charles Kittel "Introduction to Solid State Physics", chapter 13, 7th edition, John Wiley and Sons, Inc. (1996)
4. M.E. Lines and A.M. Glass "Principles and Applications of Ferroelectrics and Related Materials", chapter 4, Oxford university Press, (1977)
5. R. Landauer, J. Appl. Phys. 28, 227 (1957)
6. R.C. Miller and C. Weinreich, Phys. Rev. 117, 1460 (1960)
7. L. Ouvrad, M. Troost, Compt. Rend. 121, 117 (1890)
8. J.D. Bierlein, A Ferretti, L.H. Brixner, and W.Y. Hsu, Appl. Phys. Lett. 50, 1216 (1987)
9. C.J. van der Poel, J.D. Bierlien, J.B. Brown, and S. Colak, Appl. Phys. Lett. 57, 2074 (1990)
10. C. Canalias, J. Hirohashi, V. Pasiskevicius, and F. Laurell, J. Appl. Phys. 97, 12415 (2005)
11. S. Kim and V. Gopalan, J. Appl Phys 90, 2949 (2001)
12. P.A. Thomas and A.M. Glazer, J. Appl. Crstallogr 24, 968 (1991)
13. K. Zhang and W. Wang, Chinese Science Bulletin 46, 2028 (2001)
14. J.D. Bierlein and H. Vanherzeele, J. Opt. Soc. Am B/Vol. 6, No. 4 (1989)
15. G. Hansson, H. Karlsson, S. Wang, and F. Laurell, Appl. Opt. 39, 5058 (2000)
16. V. Yanovski and Voronkova, Phys. Status Solid. A 93. 665 (1986)

17. P.A. Morris, J. Crys. Growth 106, 76 – 88 (1990)

18. P.A. Morris, A. Ferretti, and J.D. Bierlein, J. Crys. Growth 109, 367 (1991)

19. P. Urenski and G. Rosenman, J. Mater. Res., Vol. 16, No. 5, May 2001

20. P. Urenskii, M. Molotskii, and G. Rosenman, Appl. Phys. Lett. 79, 18 (2001)

21. G. Rosenman, A. Skliar, M. Oron and M. Katz, J. Appl. Phys. 30 (1997)

22. Canalias, Doctoral Thesis, Laser Physics and Quantum Optics, Royal Institute of Technology, Stockholm (2005)